Hydrodynamic Study of a bioinspired Unmanned Underwater Vehicle by Computational Fluid Dynamics.

MARINE 2023

R. Bardera Mora[1]*, A.A. Rodriguez-Sevillano[2]†, E. Barroso Barderas[3]* and J.C. Matias García[4]*

* Instituto Nacional de Técnica Aeroespacial (INTA)
Torrejon de Ardoz, Madrid, Spain, 28850.
e-mail: barrosobe@inta.es.

† Escuela Técnica Superior de Ingeniería Aeronáutica y del Espacio (ETSIAE-UPM)
Madrid, Spain, 28040.
e-mail: angel.rodriguez.sevillano@upm.es.

ABSTRACT

This paper provides a detailed Computational Fluid Dynamics (CFD) study of the hydrodynamic characteristics of a bioinspired Unmanned Underwater Vehicle (UUV) for ocean exploration and seafloor mapping in Spain. This vehicle is intended to simulate the underwater movement of a manta ray through its Zimmerman configuration. With 1 m of wingspan, this UUV (Unmanned Underwater Vehicle) can swim with a velocity of 0.5 m/s. The design methodology used to develop this vehicle is based on the generation of a 3D CATIA model, which is divided into three main parts. The streamlined body is composed of Whitcomb II airfoils to accommodate all the electronic components, the pectoral fins are made of Eppler 61 airfoils to provide up/down or forward thrust, and the tail is represented as the body elongation to increase the vehicle manoeuvrability. The CFD study is completed with several iterations to come up with an efficient model. This numerical analysis gives a deeply understanding of hydrodynamic characteristics of this UUV that will lead to manufacture a real demonstrator in the future.

Keywords: CFD, Zimmerman wing, UUV, Bioinspired.

NOMENCLATURE

b	=	pectoral fin span
c_{max}	=	maximum pectoral fin chord
d	=	body width
C_D	=	drag coefficient
C_{Dmin}	=	minimum drag coefficient
C_f	=	skin friction coefficient
C_L	=	lift coefficient
C_{Lmax}	=	maximum lift coefficient
C_p	=	pressure coefficient
D_h	=	dihedral angle
F_D	=	lift force
F_L	=	drag force
F_y	=	side force
l	=	body length
M_x	=	roll moment
M_y	=	pitch moment
M_z	=	yaw moment
S	=	pectoral fin area

U_∞	=	freestream velocity
x	=	streamwise direction
y	=	spanwise direction
z	=	normal direction
ρ	=	freestream density
α	=	angle of attack
β	=	angle of sideslip
μ	=	dynamic viscosity
AR	=	aspect ratio
E	=	hydrodynamic efficiency

1. INTRODUCTION

Unmanned Underwater Vehicles (UUV) play a key role in many scientific and military activities such as seafloor mapping, ocean exploration, deep water mining, geophysical data collection, search and rescue operations or intelligence, surveillance and reconnaissance missions (ISR). These vehicles can operate in the deepest waters of the ocean where there are regions of dangerous or difficult human access, making them an essential resource for ocean exploration [1]. They are equipped with several sensors and high resolution cameras that allow them collect data of seafloor composition, depth level or temperature among others, and take images or record video of the seafloor. Generally, ocean exploration or seafloor mapping missions require an autonomy of several hours, so these vehicles are often powered by Li-Ion batteries, and the use of their power must be kept to a minimum to ensure a successful mission [2]. Battery power is mainly lost due to water resistance in the movement of the UUV. The design of vehicles with marine animal shapes has advantages, particularly in cases where the performance of the animal is superior to that of conventional technology [3,4]. Manta Rays are the main focus of several research project carried out by engineers and biologists due to they swim faster and more efficiently and have high maneuverability [5, 9]. When a manta ray is flapping, its movement is highly efficient as its propulsion involves very low flow energy losses. The gliding movement of a manta ray implies an important energy saving. The design methodology of a UUV can be approached from different perspectives depending on the selected design requirement: overall shape of the vehicle, propulsion system, stability, materials or movement patterns of the vehicle. A detailed understanding of the hydrodynamic performance of the UUV will lead to optimize its design through experimental and/or numerical data.

In recent years, the development of high performance computers and numerical codes has made it possible to obtain with high accuracy the velocity and pressure fields of flows on unmanned underwater vehicles. Computational Fluid Dynamics (CFD) simulation based on Reynolds Averaged Navier-Stokes (RANS) equations are gaining acceptance as a reliability prediction analysis tool for the hydrodynamic performance of underwater vehicles. Compared to experimental methods in water or wind tunnels, CFD analysis based on RANS requires less time and cost in the set-up of numerical simulations of the model. There are other numerical methods such as Large Eddy Simulation (LES) or Direct Numerical Simulation (DNS) which require to have access to supercomputers with large number of processors and huge computational memory to calculate the 3D problems [10]. However, CFD based on RANS requires less computational cost due to the mesh structures to capture the boundary layer and the time-step to solve the simulation are not as stringent. From this reason, CFD based RANS simulations to predict the hydrodynamic coefficients of an unmanned underwater vehicle seems to be a good starting point in the conceptual design phase [11].

In this paper, the initial design phase of an Unmanned Underwater Vehicle (UUV) inspired on a specific manta ray for ocean exploration missions is presented. A complex 3D model is designed to emulate the configuration of the Tainura grabata through a streamlined body and pectoral fins. Numerical simulations at different angles of attack are performed by using computational fluid dynamics (CFD). The hydrodynamic parameters and the velocity flow fields are presented to understand in detailed the behaviour of this underwater vehicle and colect data for future experimental tests in the water tunnels of the Instituto Nacional de Técnica Aeroespacial (INTA).

2. BIOINSPIRED UNMANNED UNDERWATER VEHICLE

The bioinspired Unmanned Underwater Vehicle (UUV) was designed between Instituto Nacional de Técnica Aeroespacial (INTA) and Universidad Politécnica de Madrid (UPM) for ocean exploration and seafloor mapping missions with scientific purposes in Spain. The design of this vehicle is divided into three major parts: pectoral fins, tail and body (see Figure 1). Pectoral fins provide desired forward, upward or downwards thrust to the vehicle, tail increases manoeuvrability and stability and finally body accommodates all electronics components (batteries, transmitters, velocity controller, etc) needed for the desired ocean mission.
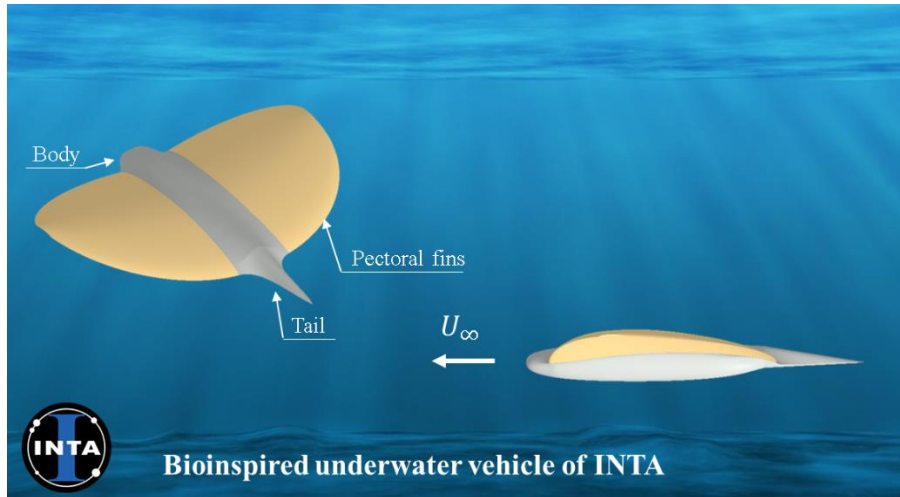
Figure 1. Bioinspired Unmanned Underwater Vehicle (UUV).

Drag reduction is one of the most important requirements during conceptual design of unmanned underwater vehicles. For this reason, the conceptual design of this vehicle has focused on minimising the drag force as much as possible during maneuvering through its streamlined configuration of body and pectoral fins that are composed each of them of different aerodynamic airfoils. The pectoral fins are designed by Eppler 61 airfoils and the body, central region, is composed of Whitcomb II airfoils. The complex junction between the pectoral fins and the body forms a smooth and continuous final surface that improves the efficiency of the vehicle.

The design of this vehicle is intended to simulate the underwater movement of a specific specie of the manta ray families through its Zimmerman configuration: Taeniura grabata (see Figure 2). This type of manta ray is tipical of Canarian islands and south of Spain which present dimensions between 1.5 and 2.5 meters and weight around 150 kg. A small scale version with a length and a wingspan of 1 meter was agreed upon as an initial test case.
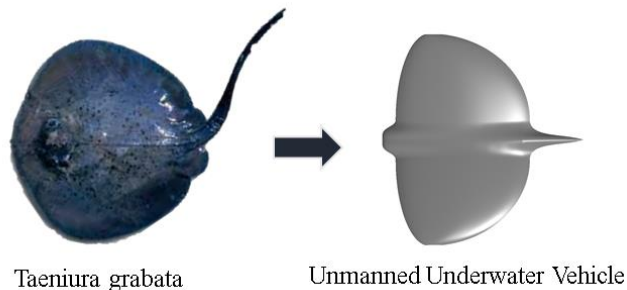

Figure 2. Unmanned Underwater Vehicle (right) of INTA inspired on the Taeniura grabata (left).

By considering the planform of the Taeniura grabata (Figure 2), a Zimmerman planform for our vehicle was selecetd. This planform consists of a joint between two halves ellipses at one point. For one half elipse that point coincide at ¼ of the maximum pectoral fin chord ($c_{max} = 625 \, mm$) amd for the seconf half elipse that

point is at ¾c_{max}. Figure 3 shows the airfoil of the pectoral fins (Eppler 61) and its Zimmerman planform with the dimensions in milimiters, and also the whitcomb-II airfoil of the UUV body.
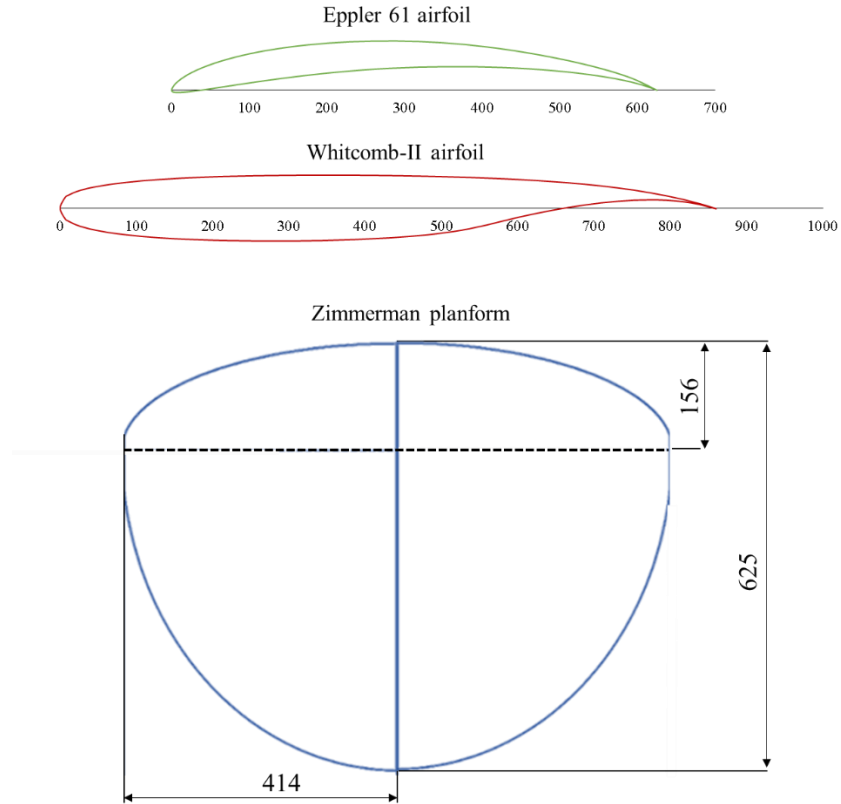

Figure 3. Airfoils of the UUV and Zimmerman planform of the pectoral fins.

The geometrical features of the Unmanned Underwater Vehicle (UUV) are summarized in Table 1.

Table 1. Geometrical features of the UUV.

Parameter	Value
Maximum pectoral fin chord, c_{max}	0.625 m
Aspect ratio, AR	2.5
Pectoral fin span, b	1 m
Pectoral fin area, S	0.4 m^2
Dihedral angle, D_h	10°
Body length, l	0.86 m
Body width, d	0.172 m

3. HYDRODYNAMIC PARAMETERS

There are four types of forces acting on an underwater vehicle: lift, drag, skin friction and pressure. All of these can be expressed by specific coefficients known as hydrodynamic parameters which are defined as the following. Firstly, the lift coefficient is given by:

$$C_L = \frac{F_L}{\frac{1}{2}\rho S U_\infty^2} \tag{1}$$

4

Where F_L is the lift force acting on the body of the vehicle in Z direction (Figure X), ρ is the sea water density which is $1030\ kg/m^3$, S is the projected area of the pectoral fins toward the Z direction and U_∞ is the freestream velocity of the flow which is $0.5m/s$. The projected area S needs to be maximized in order to obtain high lift coefficient. Because of this reason, many of the innovative designs of this type of vehicles are focusing on streamlined body shapes. That is the case of our bioinspired vehicle with a streamlined body composed of Whitcomb II airfoils. In Figure 4 there is a scheme of the UUV with the forces and moments acting on it.
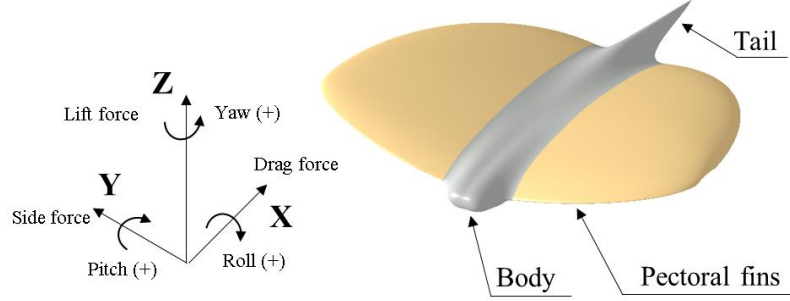

Figure 4. Forces and moments acting on the bioinspired Unmanned Underwater Vehicle.

The drag coefficient can be defined as follow:

$$C_D = \frac{F_D}{\frac{1}{2}\rho S U_\infty^2} \tag{2}$$

Where F_D is the drag force acting on the body of the vehicle in X direction (Figure 4) which needs to be as minimum as possible in order to improve the hydrodynamic of the underwater vehicle. The pressure coefficient can be defined by the following expression:

$$C_p = \frac{p - p_\infty}{\frac{1}{2}\rho U_\infty^2} \tag{3}$$

Where p_∞ is the freestream pressure and p is the pressure where the pressure coefficient is obtained. This pressure coefficient has a different value depending on the point in the flow field. When $C_p = 0$, then the pressure is the freestream pressure ($p = p_\infty$) and when the pressure coefficient is equal to the unit, then the stagnation pressure is obtained. The last hydrodynamic parameter is the skin friction coefficient C_f which is calculated as:

$$C_f = \frac{\tau_w}{\frac{1}{2}\rho U_\infty^2} \tag{4}$$

Where τ_w is the skin shear stress on the wetted body vehicle surface and it takes place when there is viscosity in the fluid. It represents the opposing force in a fluid with a moving body. The value of the skin friction coefficient is usually represented by Reynolds number, which is the ratio between inertia force and viscous force. In general, streamlined bodies provide less skin friction stress than rough surface bodies. Reynolds number, Re is given by

$$Re = \frac{\rho U_\infty L}{\mu} \tag{5}$$

Where L is the characteristic length of the vehicle and μ the dynamic viscosity of the flow.

4. COMPUTATIONAL FLUID DYNAMICS (CFD) ANALYSIS

This section contains the 3D model, meshing process and simulation specifications for the computational fluid dynamic analysis of the bioinspired underwater vehicle.

4.1 3D geometry

The bioinspired underwater vehicle, see in Figure 5, that is part of an innovative project between INTA and UPM, is in the first design phase, necessary to develop in the future a real demonstrator that can operate in oceanic missions of visual inspection by high resolution cameras and/or mapping of risky areas. The complex 3D model is generated by CATIA. The wingspan (b) and length (l) of the model are 1000 mm and 860 mm, respectively.
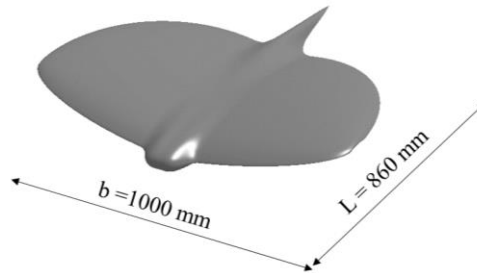
Figure 5. 3D model view in CATIA with its dimensions in milimiters.

4.2 Meshing process

A proper meshing process is required to obtain high accuracy in flow solutions. The mesh was built by ANSYS meshing tool (see Figure 6). The spatial discretizatioin of the computational domain demands an appropriate growth rate of cells, where the region near the surface of the vehicle needs to be refined with smaller cell sizes thus the velocity variations close the boundary layer can be detected. The computational domain is generated by an unstructured mesh where the cells take tetrahedral forms in all domain. The starting cell size is 20 mm and the growth rate is 1.2. The surface of the vehicle is refined by 10 mm cell size. The generated mesh has approximately a total of 5 millions elements is each simulation. This meshing criterion was selected according to an independent mesh analysis [12], in which the authors obtained the mean force coefficients using meshes with different numbers of nodes. Thus, one mesh had about 9 million nodes and the other was a finer mesh with 13 million nodes. The results obtained for the coefficients differed by less than 1.5%, concluding that a mesh of approximately 4 millions was sufficient to obtan accurate results.
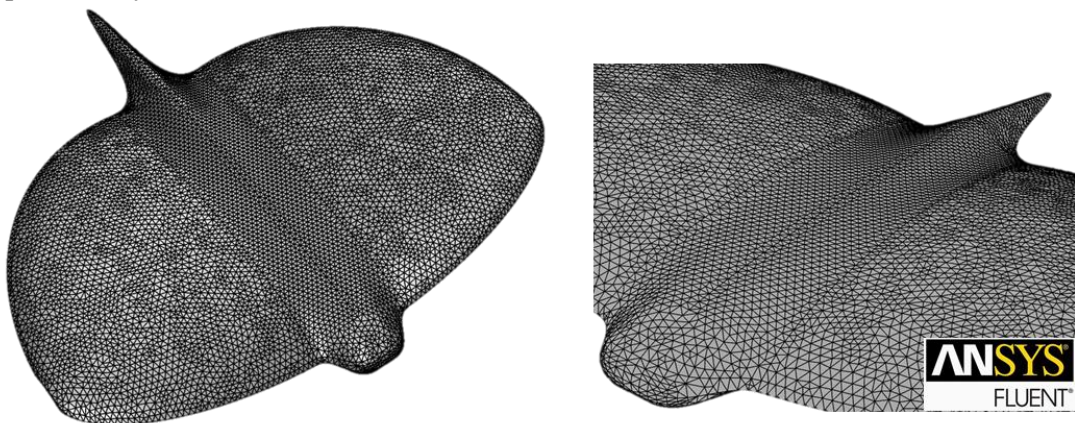

Figure 6. Bioinspired Unmanned Underwater Vehicle meshing.

In Figure 7, the dimensions of the computational flow domain with the body coordinate system for the straight-line maneuver (cruise condition, $\alpha = 0°$) are presented. All boundaries were placed far away thus avoiding blockage of the flow and negative boundary effects on the numerical solution. Therefore, the length of the

computational domain was set to a distance of 10b aft, 2b forward and 1b at the sides of the model, as can be seen in Figure 7. Because of this, the meshing load can be significantly reduced while at the same time we can ensure that the wake velocity and pressure fields generated by the vehicle are sufficiently resolved within the flow domain. As the freestream velocity is along the x-direction, and there is no propeller on the vehicle, only half of the model is computed based on the symmetry boundary with the advantage of reducing computational cost and time. The side, top and bottom boundaries are walls, the aft boundary represents the inlet velocity ($U_\infty = 0.5\ m/s$) and the forward boundary is the outlet pressure.

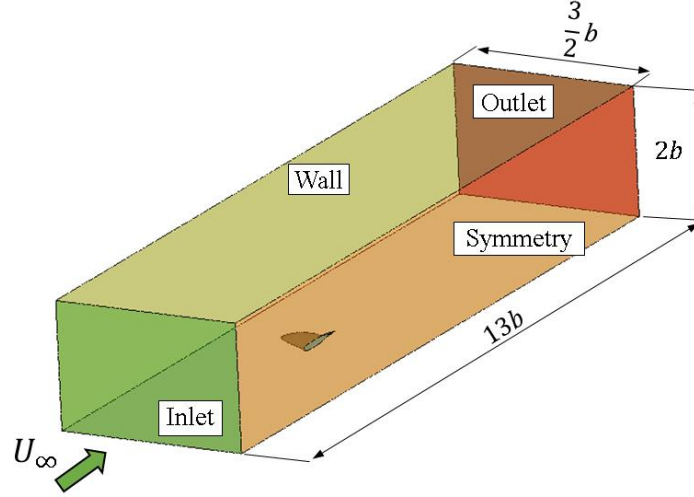**Figure 7.** Dimensions of the computational domain.

4.3 Simulation setup

The numerical simulations were performed in 3D realist scale of the model, but only half of it in order to minimize the computational time and reduce the time in finding the three dimensional solution.

The flow dynamic is represented by Navier-Stokes equations fo the velocity and pressure fields (6) and continuity (mass conservation) equations (5), respectively [10]:

$$\frac{\partial}{\partial t}\rho + \nabla \cdot (\rho u) = 0 \tag{5}$$

$$\rho \frac{Du}{Dt} = f - \nabla p + \mu \nabla^2 u \tag{6}$$

The computational fluid domain was considered as sea water with a density of $1030\ kg/m^3$ and a dynamic viscosity of $0.0009\ kg/(m \cdot s)$ at a reference temperature of $15°C$. The bioinspired unmanned underwater vehicle was analyzed under static state flow condition and incompressible regime using the commercial CFD code ANSYS-Fluent. The sea water flows over the UUV which is inside the closed sea water domain with an inlet velocity of domain $0.5\ m/s$. The Reynolds number based on the maximum pectoral fin chord ($c_{max} = 0.675\ m$) is $Re = \frac{\rho \cdot U_\infty \cdot c_{max}}{\mu} = 3.86 \cdot 10^5$.

The SST $k - \omega$ computational model was selected to analyze the hydrodynamic characteristics of the vehicle due to this model has been able to predict with high accuracy the flow along underwater vehicles. This turbulence model uses two transport equations to solve the specific dissipation rate and the turbulence kinetic energy. In the near wall region the $k - \omega$ model is applied while in the far field the $k - \varepsilon$ model is used [13]. The CFD simulations are initialized by using the sea water free-strem velocity of $0.5\ m/s$ in the inlet boundary. Running each simulation takes approximately 5 hours.

5. DISSCUSION OF RESULTS

In this section, the hydrodynamic parameters along with the velocity flow field over the Unmanned Underwater Vehicle obtained by CFD simulations are presented.

5.1 Hydrodynamic forces: lift and drag forces.

In Figure 8 the curves of lift (F_L) and drag (F_D) forces as a function of the angle of attack (α) are presented. As the objective of this paper is to increase the overall hydrodynamic performance of the vehicle, the generated lift and drag forces must be reduced. The drag force in the positive X direction opposes to the forward motion of the UUV and reduces its hydrodynamic efficiency while high lift (in Z direction) requires more thrust to propel and dip under the water. Keeping in mind these concepts, the stable and efficient forward movement of the vehicle UUV requires low values of drag and lift.

It is obvious from the simulation results that the highest force generated in the forward movement of the vehicle is the lift force (blue curve) followed by drag force (red curve). The lift force increases linearly with low angles of attack (α) until it reaches a maximum value corresponding to 80 N at 20°; beyond this angle of attack, the vehicle cannot continue operating because it has reached the stall condition. The drag force also increases with angle of attack, the maximum value being 30 N at 25°. As the vehicle cannot operate at this angle, the maximum value of drag is approximately 23 N at 20°. In the cruise condition ($\alpha = 0°$) the lift force is 10 times higher than the drag force being lift force equal to 20 N.

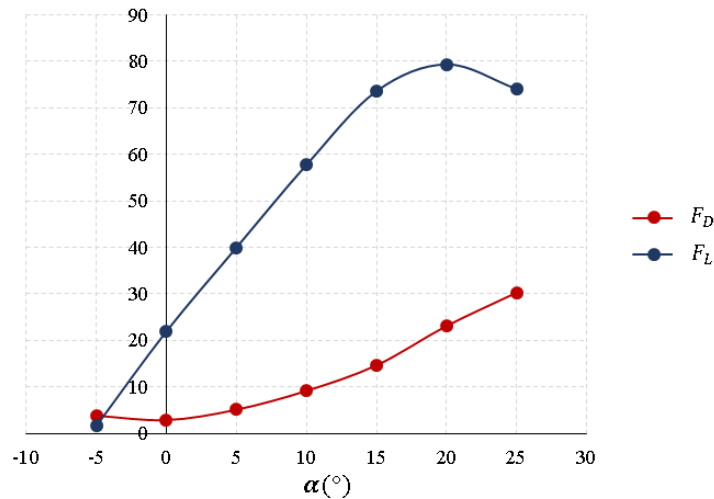**Figure 8.** Hydrodynamic forces acting on the UUV.

5.2 Pitch moment

In Figure 9 the curve of pitch M_y moment as a function of the angle of attack is presented. This hydrodynamic moment is calculated in the pressure center in two different sections: one is at the symmetric axis ($P_{C.P.2}$) and the other is at the half of the semi-pectoral fin (which is equal to $b/4$ from the symmetric axis, $P_{C.P.1}$).
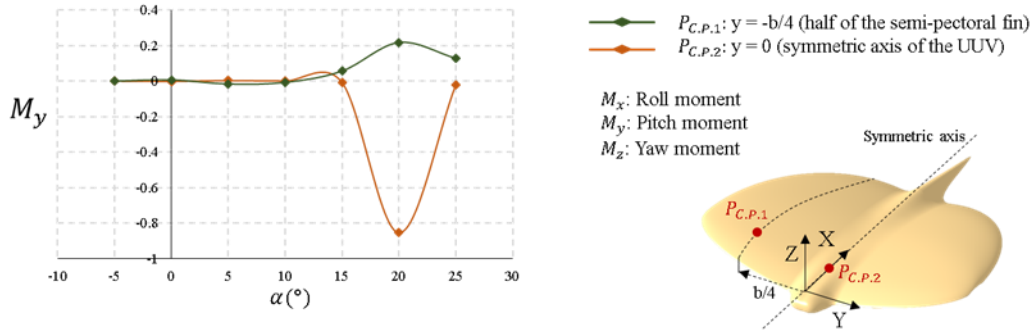
Figure 9. Hydrodynamic moments acting on the UUV.

5.3 Hydrodynamic parameters : lift and drag coefficients

It is recommended that the main body of the text ends with a summary of the key conclusions. This section may include a summary of the scope and of the methodology of the article, and a detailed list of conclusions in order of importance. In Figure 10 the curves of lift (C_L) and drag (C_D) coefficients respect to the angle of attack (α) are presented. The maximum lift coefficient (C_{Lmax}) is around 1.55 for the angle of attack of 20°, and the minimum drag coefficient (C_{Dmin}) is around 0.055 at the cruise condition ($\alpha = 0°$).
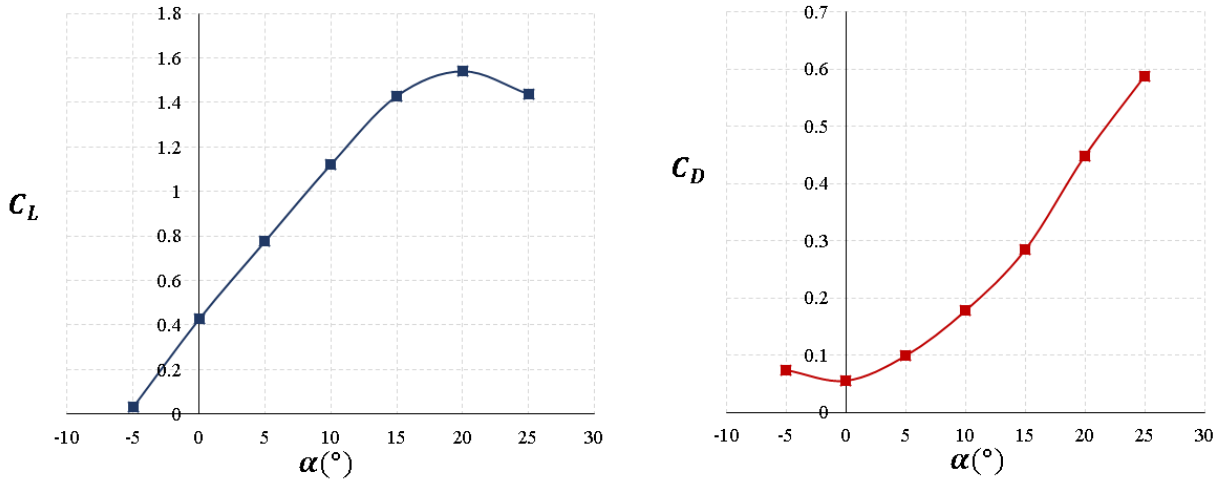

Figure 10. Lift (left) and drag (right) coefficients versus angle of attack.

5.4 Polar curve and hydrodynamic efficiency

The polar curve ($C_D - C_L$) and the hydrodynamic efficiency (E) of the unmanned underwater vehicle are presented in Figure 11. Looking at the polar curve, it can be observed that the minimum drag coefficient is around 0.055 at $C_L = 0.44$ for the cruise configuration.

The most efficient flow condition is achieved for the range of angles of attack between 0 and 5° with hydrodynamic efficiency values between 7.8 and 7.9. For higher angles of attack, the hydrodynamic efficiency drops rapidly. Angles of attack below than 0° make vehicle operation very difficult, as the hydrodynamic efficiency is less than 1when the angle of attack is −5°. The ocean exploration should be carried out with angles of attack between 0 and 5°.
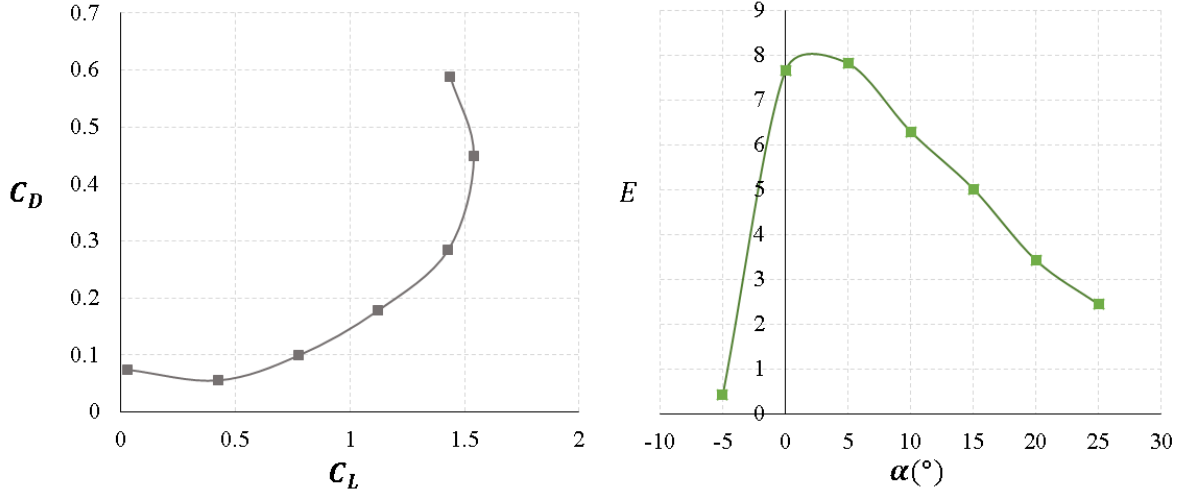
9

Figure 11. Polar curve and hydrodynamic efficiency obtained by numerical simulations.

5.5 Hydrodynamic parameters: pressure and skin friction coefficients

In Figure 12, the pressure coefficient (C_p) and skin friction coefficient (C_f) distributions over the surface of the Unmanned Underwater Vehicle (UUV) are presented, respectively.

The fluid velocity jets can give an idea of the amount of thrust production. The force required to generate the momentum change of the fluid is linked to an equal and opposite force acting on the vehicle. This force can be reflected in the pressure field that acts over the surface of the vehicle and this is presented in Figure 12 (a) for all angles of attack. The pressure field is represented by the pressure coefficient defined in equation (3) in section III. This pressure coefficient increases with the angle of attack. At low angles of attack, between $-5°$ and $5°$, there is an acceleration of the flow around the leading edge of the pectoral fins and body where the pressure drops (red region) causing leading-edge suction in that area and consequently some thrust force. From these results, the strength of leading-edge suction seems to be greater over the pectoral fins than the streamlined body of the vehicle. For higher angles of attack than $10°$, the leading-edge suction region drops. The pressure coefficient is increasing with the angle of attack.

At low angles of attack, between $-5°$ and $5°$, it is observed that the initial boundary layer flow is laminar starting from the stagnation point of the leading edge of the vehicle. In this region the skin friction is very low (dark blue region). The skin friction decreases because the flow slows down due to the adverse pressure gradient over the surface of the vehicle. When the flow accelerates at the leading edge of the vehicle, the skin friction will increase. This effect can be clearly observed at the angles of attack of $10°$ and $15°$ where there is high skin friction at the leading-edge of the body and pectoral fins (green region). The boundary layer transition from laminar to turbulent depends on the angle of attack, therefore at low angles of attack, the transition is later than at high angles of attack. After the boundary layer transition, the skin friction increases and then continues to slowly decrease as the flow slows down approaching the stagnation point of the trailing edge of the pectoral fins. The skin friction coefficient (C_f) increases with the angle of attack and high values produce high drag coefficient values. Therefore, UUV maneuvers with angles of attack greater than $5°$ will generate high drag force and hydrodynamic efficiency will decrease.
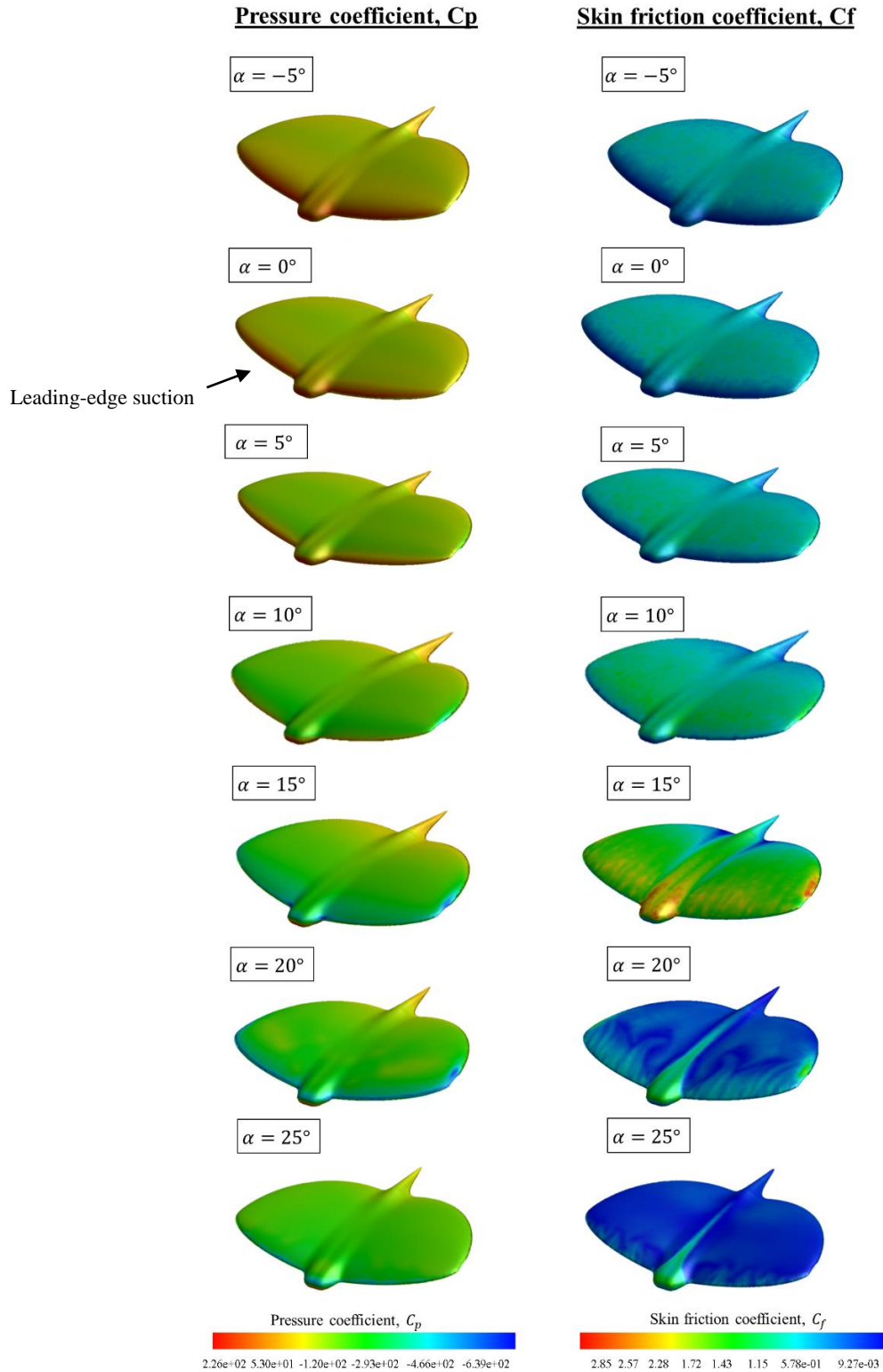
10

Figure 12. Pressure coefficient (C_p) and skin friction coefficient (C_f) distribution over the Unmanned Underwater Vehicle (UUV).

In Figure 13 the pressure coefficient contours of the inner and upper surface for the half of the semi-wing ($y = \frac{b}{4}$) is plotted for all angles of attack. The blue line represents the upper surface and the red line represents the inner surface. From these results, it can be observed that the suction peak increases with the angle of attack, reaching a maximum when the stall angle is achieved ($\alpha = 25°$).
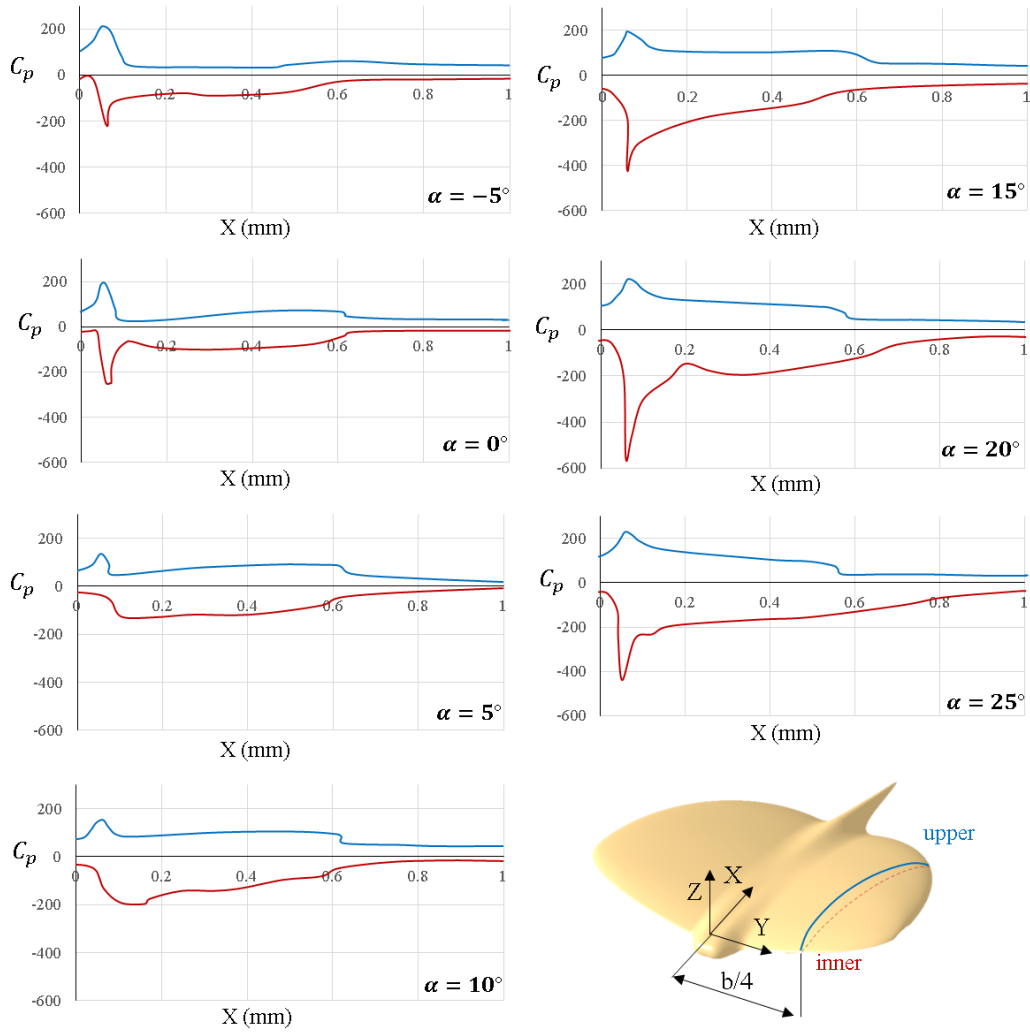
Figure 13. Pressure coefficient contours at b/4 for all angles of attack.

To obtain a detailed understanding of the flow field around the UUV, the velocity contours for all angles of attack are presented in Figure 14. The velocity field contour is obtained at the half of the semi pectoral fin ($y = \frac{b}{4}$). The orange contour shows the freestream flow velocity of $0.5 \ m/s$ while the red regions reveal the acceleration of the flow above the pectoral wing. The streamlines allow to visualize the flow attached to the pectoral fin at low angles of attack, while at high angles of attack, from $20°$ on the flow starts to be detached (blue streamlines) from fin surface reducing the hydrodynamic efficiency. At the angle of attack of $25°$, the flow is completely detached from the pectoral fin surface which makes impossible the forward motion of the vehicle. The vortex generated at the tip of the pectoral fin increases with the angle of attack. While the vortex size increases with the angle of attack, the vortex velocity decreases. For angles of attack between $5°$ and $15°$, there is an acceleration of the flow just in the tip of the pectoral fin which causes a decrease in the energy loss of the vortex that favors the vehicle's forward motion.
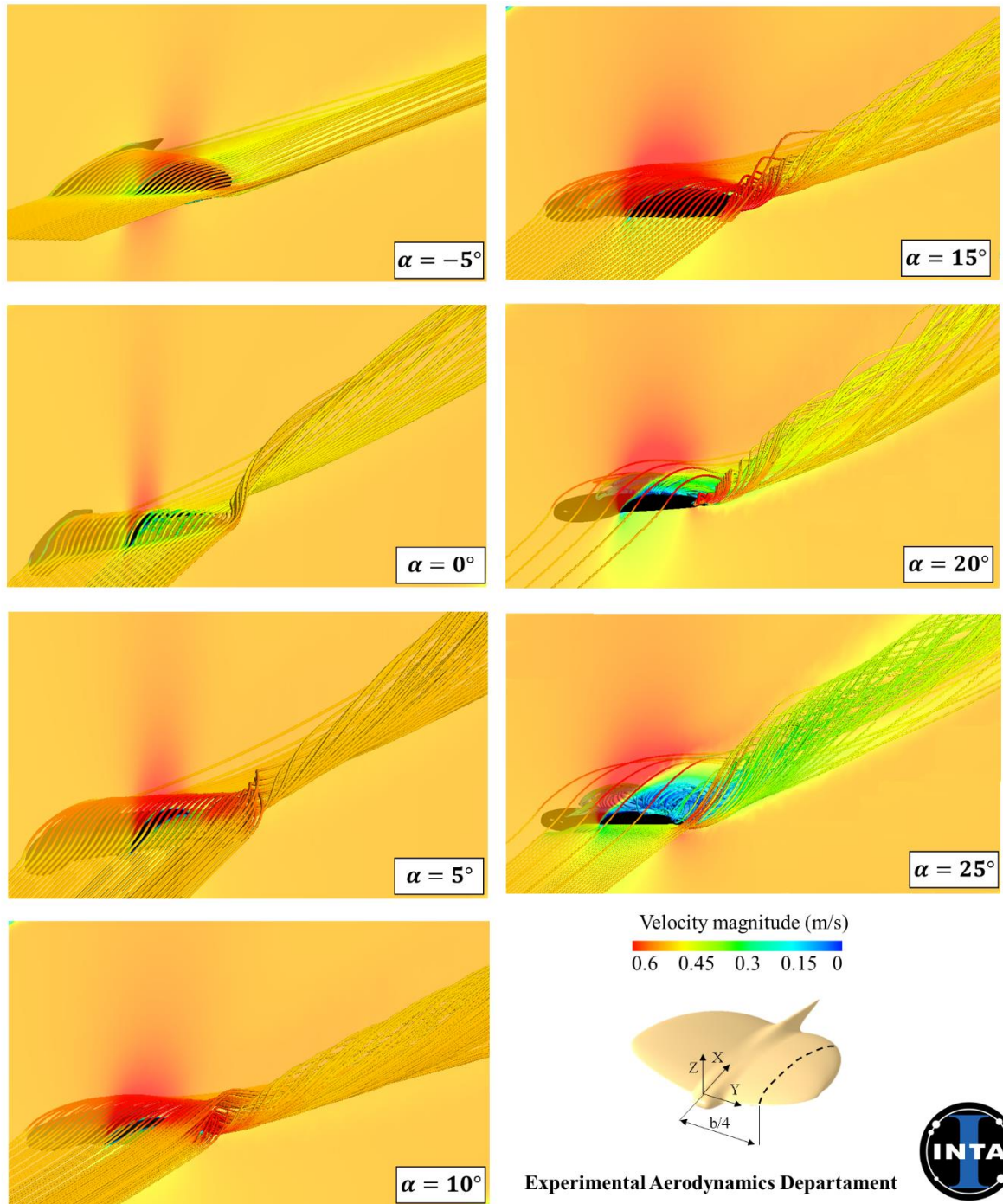
Figure 14. Velocity field at different angles of attack.

6. CONCLUSIONS

Inspiration from nature to improve the performance of underwater vehicles has been of great interest worldwide since years. In this paper, a conceptual design as close to the nature is adopted to emulate the forward movement of Manta rays. The numerical analysis provides a first estimation of detailed insight into the accurate flow dynamics of a bioinspired Unmanned Underwater Vehicle designed between INTA and UPM for ocean exploration and seafloor mapping. The design of this vehicle is intended to emulate the underwater movement of a specific manta ray: taeniura grabata; through its Zimmerman configuration. The bioinspired UUV was divided into three sections: pectoral fins, tail and streamlined body.

13

This numerical analysis give a deeply understanding of the hydrodynamic behaviour of our bioinspired UUV, being the first stage of the development process. The lift force is linear with the angle of attack until it reaches a maximum value at 25º. From this angle of attack, the stall condition is reached and the vehicle loses its functionality. The velocity contours allow to visualize the flow detachment over the vehicle and the strength of the vortex at the tip of the pectoral fin. The minimum drag is achieved for the angle of attack of 0º, and at this angle the lift has a low value, therefore the objective of low lift and drag is achieved. Finally, the hydrodynamic efficiency is maximised in the range of the angle of attack between 0° and 5°, reaching a maximum value up to 8°. Therefore, the UUV vehicle should operate within this range to optimize its hydrodynamic efficiency during the ocean exploration which could increase the autonomy

ACKNOWLEDGEMENTS

REFERENCES

[1] Wynn RB, Huvenne VA, Le Bas TP, et al. ''autonomous underwater vehicles: their past, present and future contributions to the advancement of marine geoscience'' Mar Geol 2014; 352: 451-468.

[2] Prakash J, Mitra A and Warrior HV., ''A review on the hydrodynamic characteristics of autonomous underwater vehicles'' Journal of engineering for the maritime environment, 2021, Vol 235: 15-29.

[3] Lauder GV nad Madden PG., ''Learning from fish: Kinematics and experimental hydrodynamics for roboticists'' Int J Autom Comput 2006; 3(4): 325-335.

[4] Sahoo A, Dwivedy SK and Robi P., ''Advancements in the field of autonomous underwater vehicle'' Ocean Eng 2019, 181: 145-160.

[5] Mitra S, Sehgal V, Rathore S, Puri R, Chouhan S and Sharma A, ''Design and Control Strategy of Bio-inspired Underwater Vehicle with Flexible Propulsor'', Journal of Modern Mechanical Engineering and Technology, 2021, Vol 8, 57-65.

[6] Design of a manta ray inspired underwater propulsive mechanism for long range, low power operation

[7] Singh SN, Simha A and Mittal R., ''Biorobotic AUV maneuvering by pectoral fins: inverse control design base don CFD parameterization'' IEEE J Ocean Eng 2004; 29(3): 777-785.

[8] Costa D, Palmieri G, Palpacelli MC, et al., ''Design of a Bio-Inspired Autonomous Underwater Robot'' L. Intell Robot Syst 2018; 91(2): 181-192.

[9] Honaryar A and Ghiasi M., ''Design of a bio-inspired hull shape for an AUV from hydrodynamic stability point of view through experiment and numerical analysis'', J Bionic Eng 2018; 15(6): 950-959

[10] da Cunha Lima I. C, da Silva Costa G, Ruiz A, and et.al., ''Numerical analysis of stability and manoeuvrability of Autonomous Underwater Vehicles (AUV) with fishtail shape'', Ocean Engineering, Nov 2017.

[11] Posa A and Balaras E., ' A numerial investigation about the effects of Reynolds number on the flow around an appended axisymmetric body of revolution'', J Fluid Mech 2020; 884: A41.

[12] Leong Z, Ranmuthugala D, Penesis I, et al., ''RANS-based CFD prediction of the hydrodynamic coefficients of DARPA suboff geometry in straight-line and rotating arm manoeuvres'' Int J Marit Eng 2015; 157(A1): A41-A52.

[13] Wilcox DC. ''Turbulence modeling for CFD'' Vol 2. La Canada, CA: DCW Industries, 1998.